NANO LETTERS

pubs.acs.org/NanoLett

Letter

Visualizing Heterogeneous Protein Conformations with Multi-Tilt Nanoparticle-Aided Cryo-Electron Microscopy Sampling

Changin Kim, Yeeun Kim, Sang Jin Lee, So Ri Yun, Jungkweon Choi, Seong Ok Kim, Yongsoo Yang,* and Hyotcherl Ihee*

Cite This: *Nano Lett.* 2023, 23, 3334−3343

Read Online

ACCESS | Metrics & More | Article Recommendations | Supporting Information

ABSTRACT: Obtaining the heterogeneous conformation of small proteins is important for understanding their biological role, but it is still challenging. Here, we developed a multi-tilt nanoparticle-aided cryo-electron microscopy sampling (MT-NACS) technique that enables the observation of heterogeneous conformations of small proteins and applied it to calmodulin. By imaging the proteins labeled by two gold nanoparticles at multiple tilt angles and analyzing the projected positions of the nanoparticles, the distributions of 3D interparticle distances were obtained. From the measured distance distributions, the conformational changes associated with Ca^{2+} binding and salt concentration were determined. MT-NACS was also used to track the structural change accompanied by the interaction between amyloid-beta and calmodulin, which has never been observed experimentally. This work offers an alternative platform for studying the functional flexibility of small proteins.

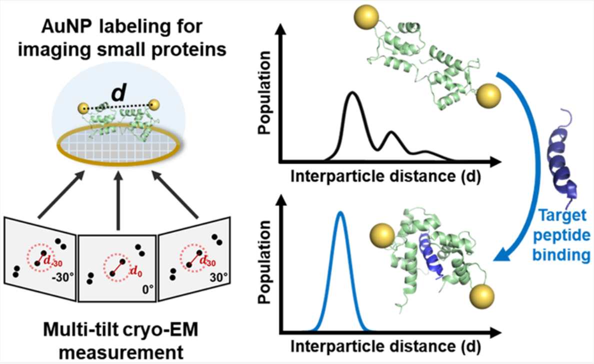

KEYWORDS: *cryo-electron microscopy, small-protein heterogeneous conformation, gold nanoparticle labeling, tilt series analysis, calmodulin*

Small proteins, typically with 100 or fewer amino acid residues (or <50 amino acids for prokaryotes and 100−200 amino acids for eukaryotes), play vital roles in critical biological processes such as protein folding, the intracellular trafficking pathway, and signal transduction.[1,2] Small proteins' flexibility and conformational plasticity allow them to effectively search for and bind with larger partner proteins to form macromolecular complexes, which is crucial for catalytic function and biomolecular recognition.[2,3] It is generally not easy to capture heterogeneous conformations of the small protein or protein complex in solution. Commonly known techniques useful for elucidating dynamic structural ensembles of proteins in the solution include nuclear magnetic resonance (NMR),[4] Förster or fluorescence resonance energy transfer (FRET), and smFRET (single-molecule FRET).[5] However, NMR, which measures average heterogeneous states, does not directly reflect individual state populations. In addition, the inherently weak signal requires high concentrations (>300 μM), preventing single-molecule measurement.[4] FRET and smFRET can provide structural information by measuring the distance between donor and acceptor fluorophores to probe interactions or movement of molecules. FRET, which extracts the average signal, cannot separate the signals of individual molecules. In contrast, the smFRET technique can characterize the distance between fluorophores of a single molecule in solution. Nevertheless, the distance at which energy transfer can occur is generally less than 10 nm for typical fluorophores, making it difficult to study domain rearrangement or orientation that undergoes large structural changes in proteins. Moreover, FRET and smFRET measurements are affected by the relative orientation of donor−acceptor pairs and the assumption of isotropic orientation distribution for the fluorophore pairs often employed by both FRET and smFRET[5] undermines the accuracy of the donor−acceptor distances, especially when the proteins are subject to preferred orientations.

As a complementary method to measure the conformational distribution of a protein based on single-object detection, we developed a nanoparticle-aided cryo-electron microscopy sampling (NACS) technique. Although small proteins are generally invisible in cryo-EM images due to low electron densities, NACS can visualize the conformational distribution of a protein via measuring the wide-range distance distribution

Received: January 26, 2023
Revised: April 3, 2023
Published: April 17, 2023

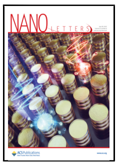

https://doi.org/10.1021/acs.nanolett.3c00313
Nano Lett. 2023, 23, 3334−3343

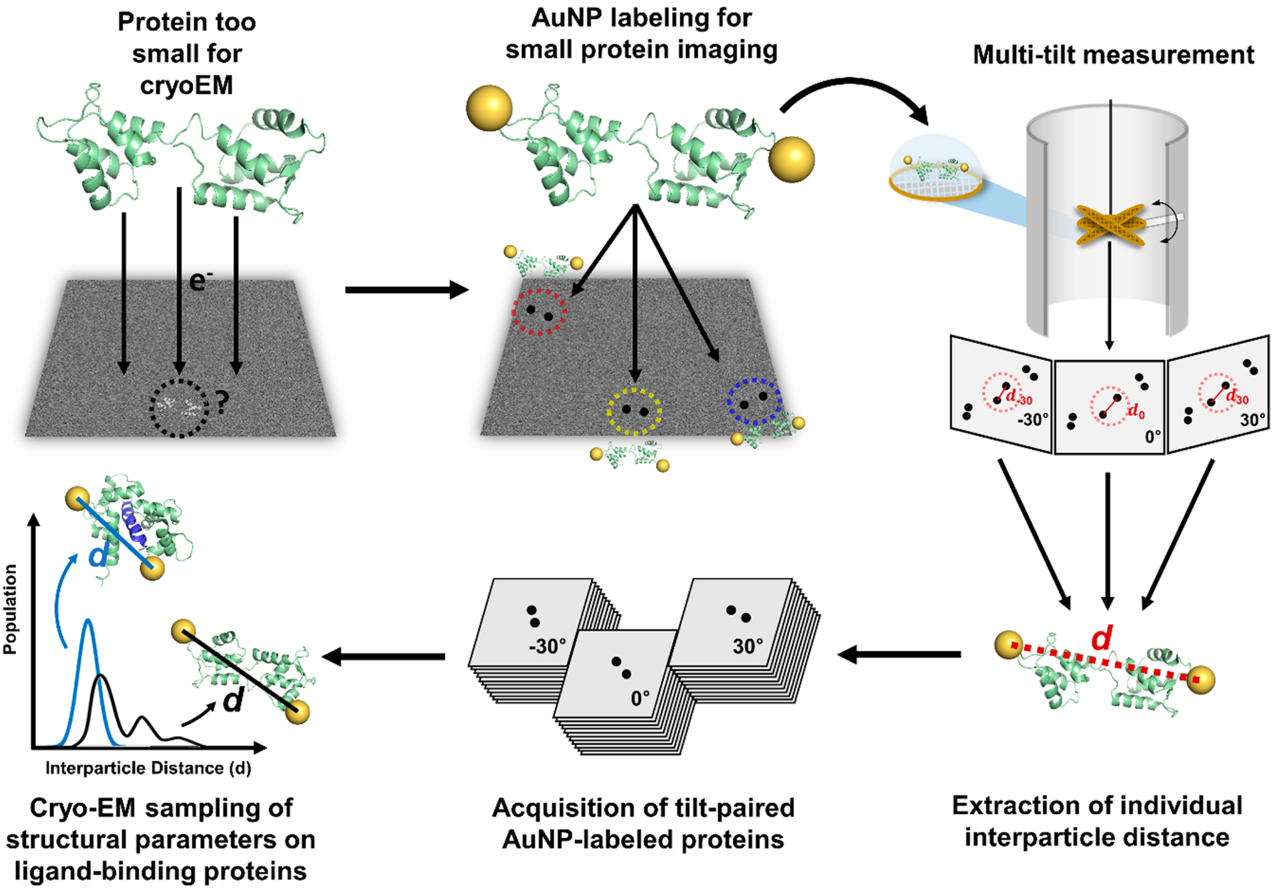

Figure 1. Schematic representation of the concept of MT-NACS (multi-tilt nanoparticle-aided cryo-EM sampling). In the MT-NACS method, gold nanoparticles (AuNPs) attached at two specific positions of the protein are measured with high contrast under cryo-EM settings at multiple tilt angles. Three-dimensional interparticle distances between two AuNPs can be directly calculated, and the distribution of instantaneous conformations of the AuNP-labeled protein can be constructed, providing the conformational distributions of proteins upon binding of ligands such as ions and peptides.

(above 10 nm) between two gold nanoparticles (AuNPs) labeled on two specific residues of the protein.[6] In the NACS technique, however, the distance distribution was obtained from images at a single angle, which only provided the projected distances between the nanoparticles. The process of extracting the actual distances required several assumptions, resulting in considerable uncertainties, which is the common limitation shared among analogous studies on other AuNP-labeled biomolecules.[7−10]

To compensate for the shortcomings of the previous studies, we have devised a multi-tilt NACS (MT-NACS) technique, which without any assumptions can directly measure the three-dimensional distance distribution between two AuNPs of an AuNP-labeled protein from cryo-EM images acquired at multiple tilt angles. Recently, the result of measuring the conformational distribution of artificial complex proteins labeled with AuNPs by taking cryo-EM images from multi-tilt angles was reported. However, for a large-sized target protein (385 kDa) that can be imaged by cryo-EM even without AuNPs was used, the advantages of using AuNPs were not fully exploited.[11]

As a model system for demonstrating the capabilities of MT-NACS, we selected calmodulin (CaM), which is too small (16 kDa) to be imaged by cryo-EM. CaM, a Ca^{2+}-binding protein, is a major mediator of calcium-regulated signal transduction pathways of eukaryotes.[12] MT-NACS was used to track the structural change of CaM in the absence and presence of Ca^{2+}. As CaM undergoes structural redistribution through specific binding motifs in CaM-binding proteins in various cellular processes,[13−15] we also used MT-NACS to investigate the structural change of CaM upon association with amyloid β-peptide (Aβ), a CaM-binding peptide. CaM binds with neurotoxic Aβ (Aβ1-42 and Aβ25-35) with high affinity and retards the rate of Aβ fibrillation.[16−18] Although the interaction between CaM and Aβ has been reported, the structural changes associated with the interaction have never been clarified through experiments. Aβ becomes larger aggregates through self-association over time, which makes it difficult to track the interaction between CaM and Aβ for a long observation. Since MT-NACS detects the frozen single molecules, it has the advantage of preventing aggregation against the long-term duration measurement. Using MT-NACS, we overcame these difficulties and succeeded experimentally in revealing the conformational distribution of apo-CaM and holo-CaM bound with Aβ25-35.

The overall process of the MT-NACS method is depicted in Figure 1. To study the conformational distribution of CaM (our target protein) using MT-NACS, the proteins should be properly labeled. First, two AuNPs were bound one by one to two specific residues of the target protein. To attach AuNPs at the target sites, the two sites were mutated with cysteine having a sulfhydryl group (Supporting Method S1). A 1.4 nm monomaleimido AuNP solution was used as a labeling reagent, so that AuNPs could be selectively attached through maleimide-reactive free thiol conjugation.[19] The monomaleimide ligand of AuNP prevents direct conjugation between CaM and AuNPs and minimizes the influence of AuNPs on CaM, thereby facilitating the measurement of conformational changes of CaM[19] (Supporting Method S2). To keep the AuNP-labeled protein in a native state in solution, a typical vitrification process used for cryo-EM measurements was performed (Supporting Method S4). After that, cryo-EM images were taken at multi-tilt angles for the AuNP-labeled protein sample. Representative images taken from three different angles (0, 30, and −30°) are shown in Figure 2.

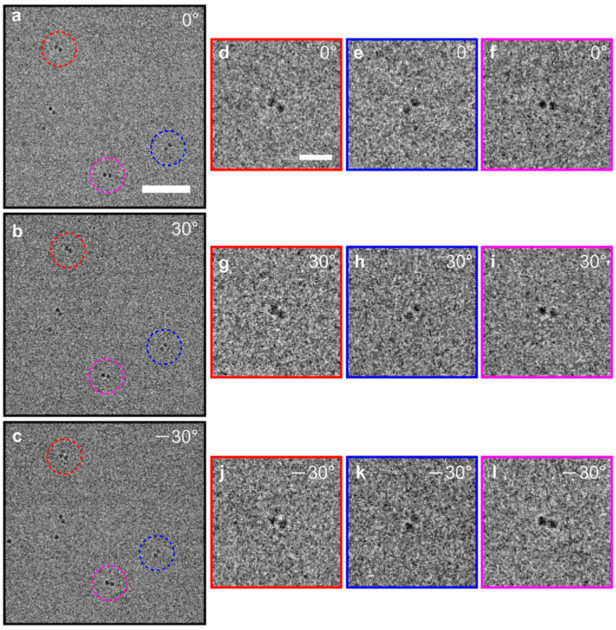

Figure 2. (a−c) Examples of cryo-EM images of CaM labeled with two AuNPs taken at three different tilt angles. Representative images of tilt angle series acquired at (a) 0°, (b) 30°, and (c) −30°. Scale bar: 30 nm. (d−f) Cropped images from the 0° image (a) near the area marked with dashed circles. (g−i) Cropped images from the 30° image (b). (j−l) Cropped images from the −30° image (c). Note that the same AuNP pairs at different tilt angles are indicated with the same color. Scale bar: 10 nm.

When an object at a reference angle (e.g., 0°) is rotated to another angle (e.g., 30 or −30°), the position projected on the $x-y$ plane can be expressed using a rotation transformation equation. The two-dimensional projected positions of the AuNPs can be obtained from each tilt image, and the three-dimensional position of the AuNPs embedded in the ice was calculated by applying the rotational transformation equation (Supporting Method S5). Using the obtained three-dimensional positions of the AuNPs, the interparticle distance, which is the distance between the two AuNPs bound to the protein, was calculated. By repeating this process for multiple AuNP-labeled proteins, the interparticle distance distribution can be obtained.

According to the reported structural information, it is known that the distance between CaM's N-terminus and C-terminus changes depending on the binding of Ca^{2+} and peptide.[20−31] Therefore, we selected the D2 position of the N-terminus and the T117 position of the C-terminus (denoted as 2-117) as the target residue sites for AuNPs binding, because they are located on the CaM surface and their inter-residue distance is directly related to the distance between the N-terminus and C-terminus (Figure 3g).

We conducted MT-NACS measurements on CaM under various sample conditions, including the presence and absence of Ca^{2+}, the salt concentration, and the presence and absence of Aβ25-35. The statistics of tracked AuNP-labeled proteins under various experimental conditions are summarized in Table S1.

AuNP-Labeled CaM with and without Ca^{2+} Binding. To investigate Ca^{2+}-induced structural changes of CaM, we measured the interparticle distance distribution before and after Ca^{2+} binding of CaM using MT-NACS under pH 6.5 and 150 mM NaCl conditions (Figure 3a,b and Table 1). Prior to MT-NACS measurements, we confirmed that CaM and AuNP-labeled CaM have similar secondary structures using circular dichroism (CD) (Supporting Method S3 and Figure S1a,b), indicating that the structure of CaM is not affected by the attachment of AuNPs. Figure 3a shows the interparticle distance distributions of AuNP-labeled CaM before and after Ca^{2+} binding obtained by MT-NACS. The distributions are asymmetric and have a long tail toward larger distance. To properly represent the asymmetricity, we used a skewed Gaussian function to fit the distribution and obtained the average and width for quantitative analysis of the distribution (Supporting Method S6). The average and width of the interparticle distance distribution for CaM before Ca^{2+} binding (apo-CaM) are 3.92 and 1.58 nm, respectively (Figure 3b and Table 1). After Ca^{2+} binding (holo-CaM), the average value decreases from 3.92 to 3.41 nm, showing that Ca^{2+} binding shortens the distance between the N-terminus and C-terminus domains. The width also decreases from 1.58 to 0.82 nm, indicating that the CaM becomes less flexible after Ca^{2+} binding (Figure 3b and Table 1).

The structural changes of CaM before and after Ca^{2+} binding measured by MT-NACS suggest that Ca^{2+} binding globally affects the structural distribution, leading to a larger population of the conformations with a shorter distance between the N-terminus and C-terminus. Various techniques, such as FRET,[20−24] smFRET,[25−30] steady-state fluorescence spectroscopy,[31] X-ray crystallography,[32−39] NMR,[40−43] and SAXS,[44−46] have been utilized to study the structural alterations of CaM upon Ca^{2+} binding. Table 1 summarizes the structural parameters obtained from these techniques for comparison with those from MT-NACS. The results from these studies are not entirely consistent.[24,25,28,31,44−46] As a result, the pattern of changes in interparticle distance distributions observed via MT-NACS aligns only with a subset of the reported outcomes. Several FRET studies[20−23] have reported a decrease in inter-fluorophore distance between the two globular domains (N-terminus and C-terminus) upon Ca^{2+} binding, although not all studies have observed the same phenomenon[24] (Table 1). The decrease was also observed in a number of smFRET studies,[26,27,29,30] while some smFRET studies report the opposite behavior.[25,28] These FRET and smFRET data suggest that the distance between the two globular domains decreases after Ca^{2+} binding, supporting the credibility of the MT-NACS method. However, we also find some inconsistencies between our results and some of the available data. For example, even the smFRET results supporting our average distance behavior show either an increase or no change in the width of the distance distribution

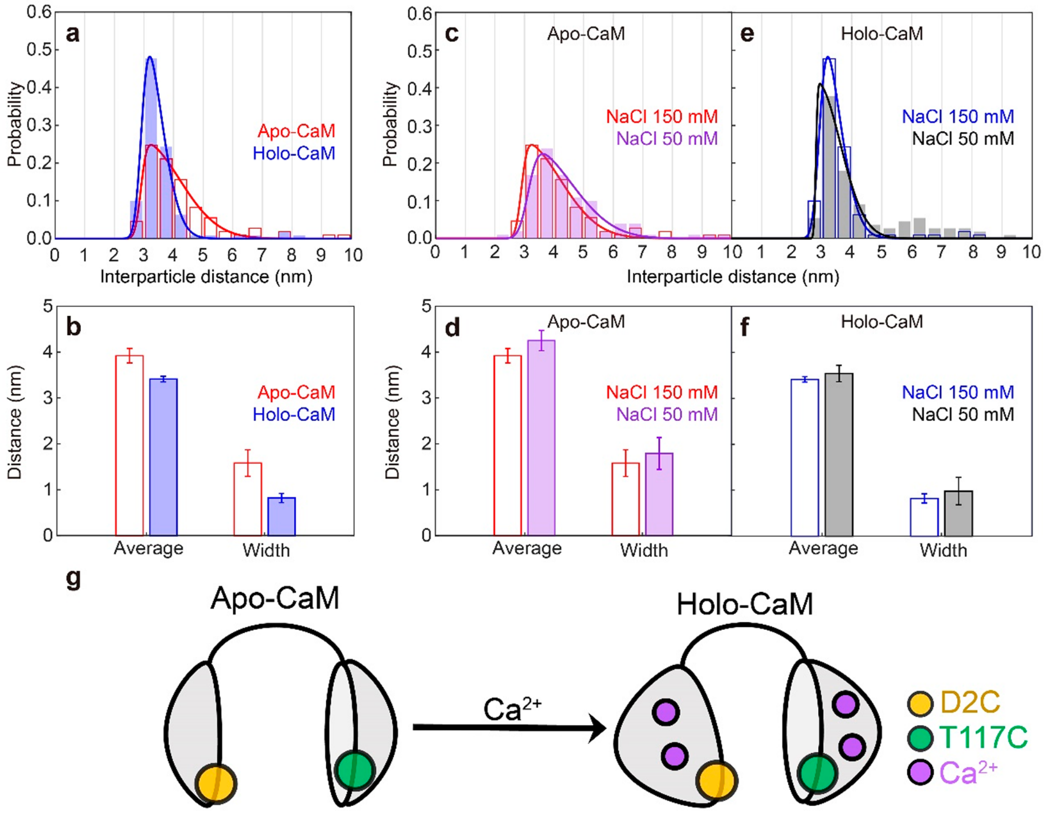

Figure 3. Structural change of CaM due to Ca^{2+} binding under two different salt concentrations probed by MT-NACS. (a, b) Interparticle distance distributions (a) and their averages and widths (b) for apo-CaM (red) and holo-CaM (blue) under 150 mM NaCl condition. (c, d) Interparticle distance distributions (c) and their averages and widths (d) of apo-CaM under 150 mM NaCl (red) and 50 mM NaCl (purple) conditions. (e, f) Interparticle distance distributions (e) and their averages and widths (f) of holo-CaM with 150 mM NaCl (blue) and 50 mM NaCl (black) conditions. The bar histograms and fitted curves using skewed Gaussian functions (shown as solid lines) are plotted together in (a, c, e), and the averages and widths in (b, d, f) were obtained from the fitting results. (g) Schematic diagram showing the structural change of CaM induced by Ca^{2+} binding. The positions of residues labeled with AuNPs are indicated by yellow (D2C) and green (T117C) circles.

upon the Ca^{2+} binding.[25−30] This is in contrast to the MT-NACS results. The structures from X-ray crystallography[32−39] and NMR[40−43] also appear to contradict the MT-NACS data; the crystal structures suggest a longer 2-117 inter-residue distance upon Ca^{2+} binding, and the inter-residue distance distributions of holo-CaM determined with NMR[40−43] are broader than those of apo-CaM (Table 1 and Figure S3). These discrepancies may be partially attributed to the sample preparation conditions used for the measurements[47−50] (Table 1), as detailed in Supporting Note S1.

Moreover, the results derived from SAXS[44−46] also differ from the MT-NACS results. The reported radius of gyration (R_g) values for holo-CaM are larger than those of apo-CaM, suggesting structural expansion upon Ca^{2+} binding.[44−46] This observation may seem contradictory to the decrease of the inter-residue distance observed in some FRET and smFRET measurements as well as MT-NACS. On the other hand, the data from ion mobility mass spectrometry (IMMS) show Ca^{2+}-induced structural shrinkage,[51] contrary to the SAXS data. The inconsistency prompted us to analyze the relationship between different inter-residue distances and R_g based on previously reported NMR structures[40,42] (Supporting Method S9). We also investigated the relationship among different inter-residue distances. Our analysis indicated that (i) positive correlations exist among different inter-residue distances (Figure S9) and (ii) R_g values are also positively correlated with the inter-residue distances in general (Figure S10). However, there are instances where an increase in R_g value accompanies a decrease in inter-residue distance or distances between different residue pairs show substantial discrepancies, especially for holo-CaM. The degrees of correlation vary depending on specific pairs of inter-residue distances and the state of Ca^{2+} binding (Figure S9). Studies also suggest that simply connecting the behavior of specific inter-residue distances with overall volume can be misleading; while a FRET study shows a decrease in the inter-residue distance, rotational dynamics measurement using fluorescence anisotropy predicts increased protein volume.[20,21] These considerations confirm that relying on a single interparticle distance may not be sufficient to discern complex structural changes in a protein. The MT-NACS technique, in principle, has the potential to provide multiple interparticle distances if suitable samples labeled with AuNPs can be prepared. This could offer complementary information to other available techniques, underscoring the potential impact of MT-NACS.

A model for the structural change from apo-CaM to holo-CaM can still be constructed by integrating information from various measurements regarding the structural change upon Ca^{2+} binding. In Figure 3g, we illustrate the proposed model, which reflects the increase in protein volume and size upon Ca^{2+} binding (from SAXS[44−46] and fluorescence anisotropy measurements[20,21]) and the shortening of the distance between the N-terminus and C-terminus (from MT-NACS, FRET, and smFRET).

Table 1. Averages and Widths of Distance Distributions of CaM before and after Ca^{2+} Binding under Various Sample Preparation Conditions

measurement method	apo-CaM					holo-CaM				
	average (nm)	width (nm)	salt concn (mM)	pH	temp (°C)	average (nm)	width (nm)	salt concn (mM)	pH	temp (°C)
MT-NACS	3.92 ± 0.16	1.58 ± 0.29	150	6.5	25	3.41 ± 0.06	0.82 ± 0.10	150	6.5	25
	4.25 ± 0.22	1.79 ± 0.35	50	6.5	25	3.45 ± 0.18	0.98 ± 0.30	50	6.5	25
ensemble FRET	2.83 (2.56)[20,a]		100	7.5	25	2.24 (1.92)[20,a]		100	7.5	25
	4.07×10^4 (Å^3)[20,b]		100	7.5	25	5.04×10^4 (Å^3)[20,b]		100	7.5	25
	3.80[21,c]		100	7.5	20	3.10[21,c]		100	7.5	20
	3.60[21,c]		100	6.3	20	3.10[21,c]		100	6.3	20
	2.61[21,c]		100	5.0	20	2.67[21,c]		100	5.0	20
	4.00[21,c]		0	7.5	20	3.30[21,c]		0	7.5	20
	3.89[22,d]		100	7.5	21	3.70[22,d]		100	7.5	21
	6.66[23,e]		160	7.5	25	5.82[23,e]		160	7.5	25
	7.94[23,e]		40	7.5	25	6.02[23,e]		40	7.5	25
	4.50 (5.10)[24,f]			7.5	25	6.90 (7.14)[24,f]			7.5	25
smFRET	5.10[25,g]	0.20[25,g]	100	7.4		5.44[25,g]	0.21[25,g]	100	7.4	
	4.94[25,g]	0.15[25,g]	100	7.4		5.15[25,g]	0.24[25,g]	100	7.4	
	3.64[26,h]	0.39[26,h]	100	7.4		3.58[26,h]	0.44[26,h]	100	7.4	
	5.32[26,h]	0.72[26,h]	100	7.4		5.16[26,h]	0.86[26,h]	100	7.4	
	3.84[27,h]	0.43[27,h]	100	7.4	25	3.41[27,h]	0.48[27,h]	100	7.4	25
	5.58[27,h]	0.58[27,h]	100	7.4	25	5.66[27,h]	0.57[27,h]	100	7.4	25
	3.11[27,h]	0.38[27,h]	100	5.0	25	3.09[27,h]	0.33[27,h]	100	5.0	25
	5.95[27,h]	0.53[27,h]	100	5.0	25	5.98[27,h]	0.61[27,h]	100	5.0	25
	3.64[27,h]	0.88[27,h]	0	7.4	25					
	5.58[27,h]	0.62[27,h]	0	7.4	25					
	4.69[28,i]	0.30[28,i]	100	7.4		5.27[28,i]	0.24[28,i]	100	7.4	
						4.35[28,i]	0.60[28,i]	100	7.4	
	4.05[29,j]	0.45[29,j]	100	7.4	25	2.00[29,j]	0.46[29,j]	100	7.4	25
	2.00[29,j]	0.42[29,j]	100	7.4	25					
	5.44[30,k]	0.41[30,k]	0		25	3.04[30,k]	0.63[30,k]	0		25
						4.87[30,k]	0.57[30,k]	0		25
X-ray crystallography[l]	3.13[32]		50	6.5		2.89[33]		10	5.6	23
						4.79[34]			5.6	25
						4.79[35]		5	4.0	18
						4.79[36]		10	5.0	3.85
						4.79[37]		55	5.0	
						4.79[38]		5	5.0	4
						3.56[39]		5	5.0	4
NMR[m]	2.16[40]		100	6.3	23	5.33[42]	1.22	0	6.5	37
	2.22[40]	0.46	100	6.3	23	3.24[43]	1.98	100	7.0	32
	2.79[41]	0.72	100	7.5	25					
SAXS	1.55−1.95 (R_g)[44,n]		100	7.4	20	1.91−2.10 (R_g)[44,n]		100	7.4	20
	1.96 (R_g)[45,o]		100	7.4	23	2.13 (R_g)[45,o]		100	7.4	23
	2.22 (R_g)[46,o]		150	7.5		2.39 (R_g)[46,o]		150	6.5	

[a] The reported values for distances between the fluorophores labeled at the 27th and 139th residues. The width information is not available. The value in parentheses is for a different donor fluorophore. [b] Hydrated volume obtained from fluorescence anisotropy measurement. [c] The reported values for distances between the fluorophores labeled at the 69th and 99th residues. The width information is not available. [d] The reported values for distances between the fluorophores labeled at the 34th and 110th residues. The width information is not available. Holo-CaM showed two different distances between the fluorophores with different probabilities: 4.00 nm (75%) and 2.80 nm (25%). [e] The reported values for distances between the fluorophores labeled at the 17th and 117th residues. The width information is not available. [f] The reported values for distances between the fluorophores labeled at the 34th and 117th residues measured by time-resolved FRET. The width information is not available. The value in the parentheses is for a different pair of donor and acceptor fluorophores. [g] The distribution of distances between the fluorophores labeled at the 34th and 110th residues were estimated from the reported FRET efficiency distribution using eq S7. Two different values are available because two different acceptor fluorophores were used. [h] The reported distribution of distances between the fluorophores labeled at the 34th and 110th residues. Both apo-CaM and holo-CaM showed two peaks. [i] The distribution of distances between the fluorophores labeled at the 44th and 117th residues were estimated from the reported FRET efficiency distribution using eq S7. Holo-CaM showed two peaks whereas apo-CaM

Table 1. continued

showed one peak. [j]The distribution of distances between the fluorophores labeled at the 66th and 110th residues were estimated from the reported FRET efficiencies distribution using eq S7. Apo-CaM showed two peaks whereas holo-CaM showed one peak. [k]The distances between the fluorophores labeled at the 34th and 110th residues were estimated from the reported FRET efficiencies using eq S7. Holo-CaM showed two peaks whereas apo-CaM showed one peak. [l]The distances between the residues 2 and 117 calculated from the reported X-ray crystal structures are shown for averages. The width information is not available. [m]The averages and widths of inter-residue distance distributions (distances between residues 2 and 117) were extracted from the reported NMR ensemble structures. [n]Radius of gyration measured for various CaM concentrations. [o]Radius of gyration.

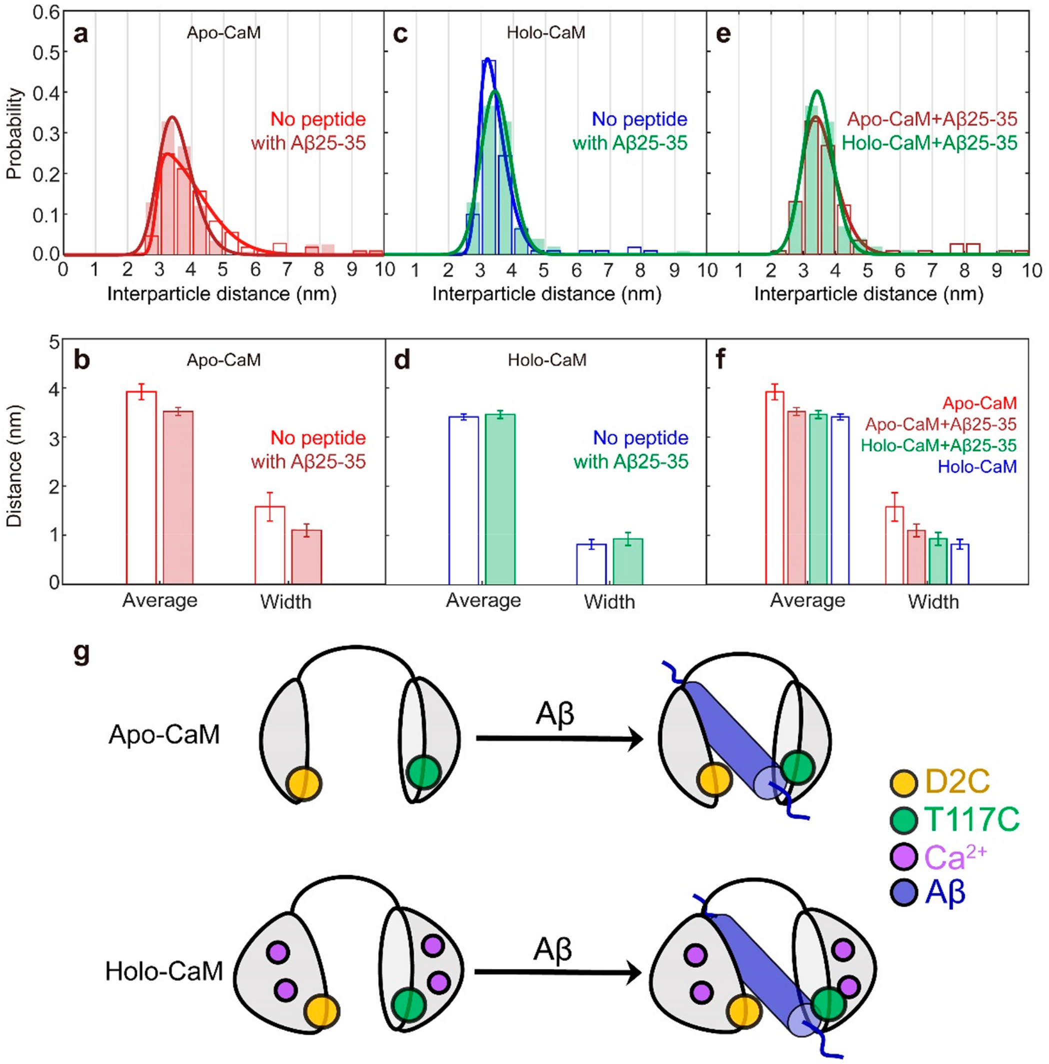

Figure 4. Structural change of CaM due to Aβ25-35 binding. (a, b) Interparticle distance distributions (a) and their averages and widths (b) for apo-CaM (red) and apo-CaM with Aβ25-35 (brown). (c, d) Interparticle distance distributions (c) and their averages and widths (d) for holo-CaM (blue) and holo-CaM with Aβ25-35 (green). (e, f) Interparticle distance distributions (e) and their averages and widths (f) for apo-CaM with Aβ25-35 (brown) and holo-CaM with Aβ25-35 (green). In (f), the averages and widths of apo-CaM and holo-CaM without Aβ25-35 were also plotted together to show that the values are similar after Aβ25-35 binding. The bar histograms and fitted curves using skewed Gaussian functions (shown as solid lines) are plotted together in (a, c, e), and the averages and widths in (b, d, f) were obtained from the fitting results. The NaCl concentration used in these measurements was 150 mM. (g) Schematic diagram showing the structural change of apo-CaM and holo-CaM upon Aβ binding unveiled via MT-NACS.

AuNP-Labeled CaM in Various Salt Concentrations. The conformation of CaM is also known to be strongly influenced by the ionic strength of the solution.[21,23,52] To check whether MT-NACS can also discern the effect of the ionic strength of the solution on the CaM structures, we performed MT-NACS measurements using a lower salt concentration (50 mM NaCl) to obtain the interparticle distance distribution of apo-CaM and holo-CaM (Figure 3c−f and Table 1). For apo-CaM, the reduced salt concentration resulted in a larger average distance (increased from 3.92 to 4.25 nm; 0.33 nm difference) compared to the 150 mM NaCl result discussed in the previous section (Figure 3c,d and Table 1). Holo-CaM does not show much dependence (increased from 3.41 to 3.45 nm; 0.04 nm difference) (Figure 3e,f and Table 1).

Table 2. Averages and Widths of Distance Distributions of CaM before and after Aβ25-35 Binding Obtained from the MT-NACS Method and MD Simulations

		apo-CaM		holo-CaM	
method		average (nm)	width (nm)	average (nm)	width (nm)
MT-NACS	no peptide	3.92 ± 0.16	1.58 ± 0.29	3.41 ± 0.06	0.82 ± 0.10
	with Aβ25-35	3.52 ± 0.08	1.10 ± 0.13	3.46 ± 0.08	0.93 ± 0.13
MD simulation	no peptide	3.03	1.86	2.87	0.73
	with Aβ25-35	2.60	0.82	2.84	0.64

The tendency of structural changes of CaM under different salt concentrations measured by MT-NACS is also consistent with the results measured by FRET[23] (Table 1). The FRET results show increased inter-fluorophore distances for both apo-CaM and holo-CaM as the KCl concentration decreases, and the difference is more pronounced for the apo-CaM case. The salt concentration dependence of the inter-domain distance can be explained in terms of the charge screening effect, as detailed in Supporting Note 2.

Since MT-NACS provides the full 3D distance distributions, the structural flexibility of a protein can also be obtained from the widths of the distance distributions. As shown in Figure 3 and Table 1, the distribution width increases for both apo-CaM (increased from 1.58 to 1.79 nm; 0.21 nm difference) and holo-CaM (increased from 0.82 to 0.98 nm; 0.16 nm difference) as the salt concentration decreases, suggesting that the structural flexibility of CaM is affected by the salt concentration of the environment.

AuNP-Labeled CaM with Aβ25-35 Binding. After the proof-of-principle verification of the MT-NACS method based on the structural changes of CaM under Ca^{2+} binding in different ionic strengths, we investigated the structural changes of CaM before and after the Aβ25-35 binding. Before actual MT-NACS measurements, we checked their binding characteristics under our experimental conditions (Supporting Note S3).

Figure 4 and Table 2 show the interparticle distance distributions of apo-CaM and holo-CaM before and after the peptide binding. When apo-CaM binds with Aβ25-35, there is a noticeable decrease in the average distance (3.92 to 3.52 nm; 0.4 nm difference) and width (1.58 to 1.10 nm; 0.48 nm difference). In contrast, holo-CaM does not exhibit significant changes in the average distance (3.41 to 3.46 nm; 0.05 nm difference) and width (0.82 to 0.93 nm; 0.11 nm difference) upon binding with Aβ25-35. The change in the average and width is more pronounced for apo-CaM compared to that of holo-CaM (Figure 4a−d and Table 2).

Since this is the first experimental observation for the conformational changes of CaM induced by Aβ25-35 binding, we performed molecular dynamics (MD) simulations to corroborate our findings (Supporting Method S7). We calculated the 2-117 inter-residue distance distributions of CaM before and after Aβ25-35 binding based on the MD snapshots (Figure 5 and Table 2). The tendency of structural change for CaM before and after the Aβ25-35 binding agrees with the experiment; the 2-117 inter-residue distance distribution of apo-CaM becomes narrower (the width changes from 1.86 to 0.82 nm; 1.04 nm difference) and shifts toward a shorter distance (the average changes from 3.03 to 2.60 nm; 0.43 nm difference) after the peptide binding. Holo-CaM shows no significant changes in their distribution (the width changes from 0.73 to 0.64 nm; 0.09 nm difference, the average changes from 2.87 to 2.84 nm; 0.03 nm difference).

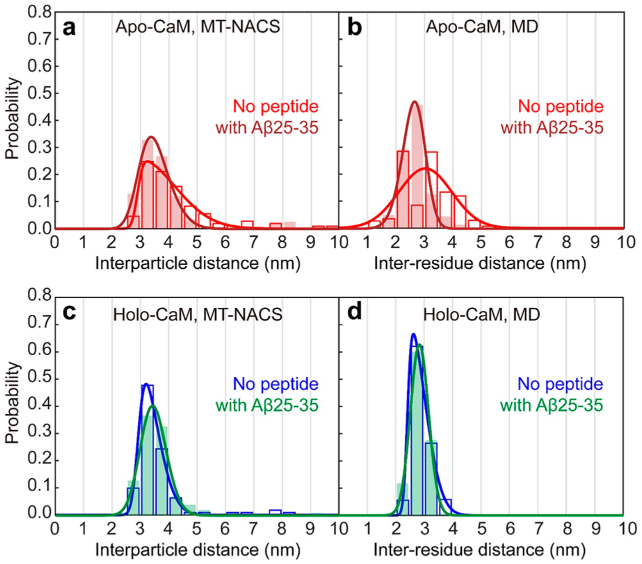

Figure 5. Comparison of distance distributions of CaM before and after Aβ25-35 binding obtained from MT-NACS and MD simulations. (a, b) Distance distributions of apo-CaM before (red) and after Aβ25-35 binding (brown) obtained from MT-NACS (a) and MD simulations (b). (c, d) Distance distributions of holo-CaM before (blue) and after Aβ25-35 binding (green) obtained from MT-NACS (c) and MD simulations (d). The bar histograms and fitted curves using skewed Gaussian functions (shown as solid lines) are plotted together. The distributions from the MT-NACS experiment and MD simulations show consistent behavior.

The experimental and simulation results together suggest that the flexible apo-CaM structure is strongly influenced by the Aβ25-35 binding, being transformed into substantially compact forms (Figures 4a,b and 5a,b and Table 2). In contrast, the compact holo-CaM structure is relatively unaffected by the Aβ25-35 binding (Figures 4c,d and 5c,d and Table 2) showing relatively little difference after Aβ25-35 binding. Consequently, apo-CaM and holo-CaM become similar compact conformations after Aβ25-35 binding, regardless of the initial structure, as evidenced in our quantitative analysis of the distributions: their averages and widths show only 0.06 and 0.17 nm differences, respectively (Figure 4e,f and Table 2).

Previous studies suggest that the structural properties (i.e., conformations) of CaM after peptide binding are highly related to the CaM−peptide interaction, strongly influencing their dissociation constants. The conformations of higher flexibility (more relaxed structures) result in relatively higher dissociation constants (a few hundred nanometers),[53−57] indicating weak interactions between CaM and peptides. In contrast, lower dissociation constants (a few tens of nanometers)[58−61] were observed for the peptide-bound-CaM of compact forms, which implies stronger interactions. In the case of CaM binding with Aβ, relatively low dissociation constants (i.e., strong interaction between them) were reported for both apo- and holo-CaM (apo-CaM, 22 nM; holo-CaM, <1 nM),[16] supporting our results of both apo- and holo-CaM exhibiting compact structures after Aβ binding (Figure 4g).

In this study, we developed a new technique named MT-NACS, which can directly quantify the conformational changes of small-sized proteins by multi-tilt cryo-EM measurements on the individual AuNP-labeled proteins. Our method is validated by measuring the 3D distance distributions between the N-terminus and C-terminus domain of CaM, before and after Ca^{2+} binding under different salt concentrations, which are in accordance with the results reported via other established techniques. We further elucidated the structural changes of CaM before and after Aβ25-35 binding, which has been difficult to achieve due to the limitations of conventional approaches. We note that the MT-NACS technique has several limitations (Supporting Note S4). Nevertheless, MT-NACS method has the potential to be a powerful tool to investigate the conformational heterogeneity and structural dynamics of biomolecules, including molecular assembly or even small flexible proteins such as aggregation-prone proteins and intrinsically disordered proteins.

ASSOCIATED CONTENT

Supporting Information

The Supporting Information is available free of charge at https://pubs.acs.org/doi/10.1021/acs.nanolett.3c00313.

> Supporting Notes for a discussion on the discrepancy between the MT-NACS data and those from X-ray crystallography and NMR, charge screening effect to explain the salt concentration dependence of the inter-domain distance, binding characteristics of CaM and Aβ25-35, and limitations of the MT-NACS technique, Supporting Methods for CaM expression and purification, AuNPs labeling of CaM, characterization of CaM and AuNP-labeled CaM with and without Ca^{2+} and Aβ, cryo-EM experiment, calculating the interparticle distances of AuNP-labeled proteins, fitting interparticle distance distribution using a skewed Gaussian function, extracting the inter-residue distance distribution from the MD-generated structures, extraction of the inter-fluorophore distance from FRET and smFRET data, and extracting the radii of gyration and inter-residue distances from NMR structures, a Supporting Table for numbers of successfully tracked AuNP pairs found for various experimental conditions, Supporting Figures for results of CD measurement, characterization of holo-CaM and Aβ25-35 (ThT aggregation assay, isothermal titration calorimetry), inter-residue distance distributions of CaM based on reported NMR structures, SEC result of AuNP-labeled CaM, schematic diagram of calculating the interparticle distances of AuNP-labeled proteins, example of the particle locating process, excluding artifacts due to crystal ice, representative cropped images of AuNP-labeled apo-CaM under the 150 mM NaCl condition, correlations between various inter-residue distances observed in reported NMR structures, and correlations between various inter-residue distances and R_g observed in reported NMR structures (PDF)

AUTHOR INFORMATION

Corresponding Authors

Yongsoo Yang − *Department of Physics, Korea Advanced Institute of Science and Technology (KAIST), Daejeon 34141, Republic of Korea*; orcid.org/0000-0001-8654-302X; Phone: +82-42-350-7303; Email: yongsoo.yang@kaist.ac.kr

Hyotcherl Ihee − *Department of Chemistry, Korea Advanced Institute of Science and Technology (KAIST), Daejeon 34141, Republic of Korea; KI for the BioCentury, Korea Advanced Institute of Science and Technology (KAIST), Daejeon 34141, Republic of Korea; Center for Advanced Reaction Dynamics, Institute for Basic Science (IBS), Daejeon 34141, Republic of Korea*; orcid.org/0000-0003-0397-5965; Phone: +82-42-350-2844; Email: hyotcherl.ihee@kaist.ac.kr

Authors

Changin Kim − *Department of Chemistry, Korea Advanced Institute of Science and Technology (KAIST), Daejeon 34141, Republic of Korea; KI for the BioCentury, Korea Advanced Institute of Science and Technology (KAIST), Daejeon 34141, Republic of Korea; Center for Advanced Reaction Dynamics, Institute for Basic Science (IBS), Daejeon 34141, Republic of Korea*

Yeeun Kim − *Department of Physics, Korea Advanced Institute of Science and Technology (KAIST), Daejeon 34141, Republic of Korea*

Sang Jin Lee − *Department of Chemistry, Korea Advanced Institute of Science and Technology (KAIST), Daejeon 34141, Republic of Korea; KI for the BioCentury, Korea Advanced Institute of Science and Technology (KAIST), Daejeon 34141, Republic of Korea; Center for Advanced Reaction Dynamics, Institute for Basic Science (IBS), Daejeon 34141, Republic of Korea*

So Ri Yun − *Department of Chemistry, Korea Advanced Institute of Science and Technology (KAIST), Daejeon 34141, Republic of Korea; KI for the BioCentury, Korea Advanced Institute of Science and Technology (KAIST), Daejeon 34141, Republic of Korea; Center for Advanced Reaction Dynamics, Institute for Basic Science (IBS), Daejeon 34141, Republic of Korea*

Jungkweon Choi − *Department of Chemistry, Korea Advanced Institute of Science and Technology (KAIST), Daejeon 34141, Republic of Korea; KI for the BioCentury, Korea Advanced Institute of Science and Technology (KAIST), Daejeon 34141, Republic of Korea; Center for Advanced Reaction Dynamics, Institute for Basic Science (IBS), Daejeon 34141, Republic of Korea*; orcid.org/0000-0002-9979-305X

Seong Ok Kim − *Department of Chemistry, Korea Advanced Institute of Science and Technology (KAIST), Daejeon 34141, Republic of Korea; KI for the BioCentury, Korea Advanced Institute of Science and Technology (KAIST), Daejeon 34141, Republic of Korea; Center for Advanced Reaction Dynamics, Institute for Basic Science (IBS), Daejeon 34141, Republic of Korea*

Complete contact information is available at: https://pubs.acs.org/10.1021/acs.nanolett.3c00313

Author Contributions

H.I. conceived the idea. H.I. and Y.Y. supervised the project. H.I., Y.Y., C.K., and Y.K. designed the experiment. C.K., S.R.Y., and S.O.K. prepared the sample. Y.Y., Y.K., and H.I. developed the data analysis strategy. C.K., and Y.K. performed the experiments. Y.K. analyzed the data. C.K., S.J.L., and S.R.Y. performed MD simulations. C.K., Y.K., S.J.L., J.C., Y.Y., and H.I. wrote the manuscript, and all authors commented on the manuscript. C.K. and Y.K. contributed equally.

Notes

The authors declare no competing financial interest.

■ ACKNOWLEDGMENTS

TEM measurements were conducted at the KAIST Analysis Center for Research Advancement (KARA), Institute for Basic Science (IBS), and EM & Histology Core Facility, at the BioMedical Research Center, KAIST. The authors thank JinSeok Choi, Seong Gyu Lee, Bumhan Ryu, and Yongsuk Hur for their dedicated support for the cryo-EM experiments. C.K., S.J.L., S.R.Y., J.C., S.O.K., and H.I. were supported by the Institute for Basic Science (IBS-R033). Y.K., and Y.Y. were supported by the Samsung Science and Technology Foundation (SSTFBA1802-05).

■ REFERENCES

(1) Steinberg, R.; Koch, H. G. The largely unexplored biology of small proteins in pro- and eukaryotes. *FEBS J.* **2021**, *288*, 7002−7024.

(2) Yang, X.; Tschaplinski, T. J.; Hurst, G. B.; Jawdy, S.; Abraham, P. E.; Lankford, P. K.; Adams, R. M.; Shah, M. B.; Hettich, R. L.; Lindquist, E.; Kalluri, U. C.; Gunter, L. E.; Pennacchio, C.; Tuskan, G. A. Discovery and annotation of small proteins using genomics, proteomics, and computational approaches. *Genome Res.* **2011**, *21*, 634−641.

(3) Su, M.; Ling, Y.; Yu, J.; Wu, J.; Xiao, J. Small proteins: untapped area of potential biological importance. *Front Genet.* **2013**, *4*, 286.

(4) Wuthrich, K. Protein structure determination in solution by NMR spectroscopy. *J. Biol. Chem.* **1990**, *265*, 22059−22062.

(5) Sasmal, D. K.; Pulido, L. E.; Kasal, S.; Huang, J. Single-molecule fluorescence resonance energy transfer in molecular biology. *Nanoscale* **2016**, *8*, 19928−19944.

(6) Ki, H.; Jo, J.; Kim, Y.; Kim, T. W.; Kim, C.; Kim, Y.; Kim, C. W.; Muniyappan, S.; Lee, S. J.; Kim, Y.; Kim, H. M.; Yang, Y.; Ihee, H. Uncovering the Conformational Distribution of a Small Protein with Nanoparticle-Aided Cryo-Electron Microscopy Sampling. *J. Phys. Chem. Lett.* **2021**, *12*, 6565−6573.

(7) Busson, M. P.; Rolly, B.; Stout, B.; Bonod, N.; Larquet, E.; Polman, A.; Bidault, S. Optical and topological characterization of gold nanoparticle dimers linked by a single DNA double strand. *Nano Lett.* **2011**, *11*, 5060−5065.

(8) Zhang, L.; Lei, D.; Smith, J. M.; Zhang, M.; Tong, H.; Zhang, X.; Lu, Z.; Liu, J.; Alivisatos, A. P.; Ren, G. Three-dimensional structural dynamics and fluctuations of DNA-nanogold conjugates by individual-particle electron tomography. *Nat. Commun.* **2016**, *7*, 11083.

(9) Chen, Q.; Smith, J. M.; Park, J.; Kim, K.; Ho, D.; Rasool, H. I.; Zettl, A.; Alivisatos, A. P. 3D motion of DNA-Au nanoconjugates in graphene liquid cell electron microscopy. *Nano Lett.* **2013**, *13*, 4556−4561.

(10) Lermusiaux, L.; Sereda, A.; Portier, B.; Larquet, E.; Bidault, S. Reversible switching of the interparticle distance in DNA-templated gold nanoparticle dimers. *ACS Nano* **2012**, *6*, 10992−10998.

(11) Jagota, M.; Townshend, R. J. L.; Kang, L. W.; Bushnell, D. A.; Dror, R. O.; Kornberg, R. D.; Azubel, M. Gold nanoparticles and tilt pairs to assess protein flexibility by cryo-electron microscopy. *Ultramicroscopy* **2021**, *227*, 113302.

(12) Chin, D.; Means, A. R. Calmodulin: a prototypical calcium sensor. *Trends Cell Biol.* **2000**, *10*, 322−328.

(13) Hoeflich, K. P.; Ikura, M. Calmodulin in action: diversity in target recognition and activation mechanisms. *Cell* **2002**, *108*, 739−742.

(14) Peersen, O. B.; Madsen, T. S.; Falke, J. J. Intermolecular tuning of calmodulin by target peptides and proteins: differential effects on Ca^{2+} binding and implications for kinase activation. *Protein Sci.* **1997**, *6*, 794−807.

(15) Tidow, H.; Nissen, P. Structural diversity of calmodulin binding to its target sites. *FEBS J.* **2013**, *280*, 5551−5565.

(16) Corbacho, I.; Berrocal, M.; Torok, K.; Mata, A. M.; Gutierrez-Merino, C. High affinity binding of amyloid beta-peptide to calmodulin: Structural and functional implications. *Biochem. Biophys. Res. Commun.* **2017**, *486*, 992−997.

(17) Poejo, J.; Salazar, J.; Mata, A. M.; Gutierrez-Merino, C. The Relevance of Amyloid beta-Calmodulin Complexation in Neurons and Brain Degeneration in Alzheimer's Disease. *Int. J. Mol. Sci.* **2021**, *22*, 4976.

(18) Hardy, J. A.; Higgins, G. A. Alzheimer's disease: the amyloid cascade hypothesis. *Science* **1992**, *256*, 184−185.

(19) Ackerson, C. J.; Powell, R. D.; Hainfeld, J. F. Site-specific biomolecule labeling with gold clusters. *Methods Enzymol.* **2010**, *481*, 195−230.

(20) Yao, Y.; Schoneich, C.; Squier, T. C. Resolution of structural changes associated with calcium activation of calmodulin using frequency domain fluorescence spectroscopy. *Biochemistry* **1994**, *33*, 7797−7810.

(21) Sun, H.; Yin, D.; Squier, T. C. Calcium-dependent structural coupling between opposing globular domains of calmodulin involves the central helix. *Biochemistry* **1999**, *38*, 12266−12279.

(22) Torok, K.; Tzortzopoulos, A.; Grabarek, Z.; Best, S. L.; Thorogate, R. Dual effect of ATP in the activation mechanism of brain Ca^{2+}/calmodulin-dependent protein kinase II by Ca^{2+}/calmodulin. *Biochemistry* **2001**, *40*, 14878−14890.

(23) Hellstrand, E.; Kukora, S.; Shuman, C. F.; Steenbergen, S.; Thulin, E.; Kohli, A.; Krouse, B.; Linse, S.; Akerfeldt, K. S. Forster resonance energy transfer studies of calmodulin produced by native protein ligation reveal inter-domain electrostatic repulsion. *FEBS J.* **2013**, *280*, 2675−2687.

(24) McCarthy, M. R.; Savich, Y.; Cornea, R. L.; Thomas, D. D. Resolved Structural States of Calmodulin in Regulation of Skeletal Muscle Calcium Release. *Biophys. J.* **2020**, *118*, 1090−1100.

(25) DeVore, M. S.; Braimah, A.; Benson, D. R.; Johnson, C. K. Single-Molecule FRET States, Conformational Interchange, and Conformational Selection by Dye Labels in Calmodulin. *J. Phys. Chem. B* **2016**, *120*, 4357−4364.

(26) Slaughter, B. D.; Allen, M. W.; Unruh, J. R.; Bieber Urbauer, R. J.; Johnson, C. K. Single-Molecule Resonance Energy Transfer and Fluorescence Correlation Spectroscopy of Calmodulin in Solution. *J. Phys. Chem. B* **2004**, *108*, 10388−10397.

(27) Slaughter, B. D.; Unruh, J. R.; Allen, M. W.; Bieber Urbauer, R. J.; Johnson, C. K. Conformational substates of calmodulin revealed by single-pair fluorescence resonance energy transfer: influence of solution conditions and oxidative modification. *Biochemistry* **2005**, *44*, 3694−3707.

(28) Devore, M. S.; Gull, S. F.; Johnson, C. K. Reconstruction of Calmodulin Single-Molecule FRET States, Dye-Interactions, and CaMKII Peptide Binding by MultiNest and Classic Maximum Entropy. *Chem. Phys.* **2013**, *422*, 238−245.

(29) Han, M. J.; He, Q. T.; Yang, M.; Chen, C.; Yao, Y.; Liu, X.; Wang, Y.; Zhu, Z. L.; Zhu, K. K.; Qu, C.; Yang, F.; Hu, C.; Guo, X.; Zhang, D.; Chen, C.; Sun, J. P.; Wang, J. Single-molecule FRET and conformational analysis of beta-arrestin-1 through genetic code expansion and a Se-click reaction. *Chem. Sci.* **2021**, *12*, 9114−9123.

(30) Sadoine, M.; Cerminara, M.; Kempf, N.; Gerrits, M.; Fitter, J.; Katranidis, A. Selective Double-Labeling of Cell-Free Synthesized Proteins for More Accurate smFRET Studies. *Anal. Chem.* **2017**, *89*, 11278−11285.

(31) Boschek, C. B.; Squier, T. C.; Bigelow, D. J. Disruption of interdomain interactions via partial calcium occupancy of calmodulin. *Biochemistry* **2007**, *46*, 4580−4588.

(32) Schumacher, M. A.; Crum, M.; Miller, M. C. Crystal structures of apocalmodulin and an apocalmodulin/SK potassium channel gating domain complex. *Structure* **2004**, *12*, 849−860.

(33) Fallon, J. L.; Quiocho, F. A. A closed compact structure of native Ca^{2+}-calmodulin. *Structure* **2003**, *11*, 1303−1307.

(34) Babu, Y. S.; Bugg, C. E.; Cook, W. J. Structure of calmodulin refined at 2.2 Å resolution. *J. Mol. Biol.* **1988**, *204*, 191−204.

(35) Taylor, D. A.; Sack, J. S.; Maune, J. F.; Beckingham, K.; Quiocho, F. A. Structure of a recombinant calmodulin from Drosophila melanogaster refined at 2.2-Å resolution. *J. Biol. Chem.* **1991**, *266*, 21375−21380.

(36) Ban, C.; Ramakrishnan, B.; Ling, K. Y.; Kung, C.; Sundaralingam, M. Structure of the recombinant Paramecium tetraurelia calmodulin at 1.68 Å resolution. *Acta Crystallogr. D Biol. Crystallogr.* **1994**, *50*, 50−63.

(37) Chattopadhyaya, R.; Meador, W. E.; Means, A. R.; Quiocho, F. A. Calmodulin structure refined at 1.7 Å resolution. *J. Mol. Biol.* **1992**, *228*, 1177−1192.

(38) Rao, S. T.; Wu, S.; Satyshur, K. A.; Ling, K. Y.; Kung, C.; Sundaralingam, M. Structure of Paramecium tetraurelia calmodulin at 1.8 Å resolution. *Protein Sci.* **1993**, *2*, 436−447.

(39) Wilson, M. A.; Brunger, A. T. The 1.0 Å crystal structure of Ca^{2+}-bound calmodulin: an analysis of disorder and implications for functionally relevant plasticity. *J. Mol. Biol.* **2000**, *301*, 1237−1256.

(40) Kuboniwa, H.; Tjandra, N.; Grzesiek, S.; Ren, H.; Klee, C. B.; Bax, A. Solution structure of calcium-free calmodulin. *Nat. Struct. Biol.* **1995**, *2*, 768−776.

(41) Zhang, M.; Tanaka, T.; Ikura, M. Calcium-induced conformational transition revealed by the solution structure of apo calmodulin. *Nat. Struct. Biol.* **1995**, *2*, 758−767.

(42) Kainosho, M.; Torizawa, T.; Iwashita, Y.; Terauchi, T.; Mei Ono, A.; Guntert, P. Optimal isotope labelling for NMR protein structure determinations. *Nature* **2006**, *440*, 52−57.

(43) Gsponer, J.; Christodoulou, J.; Cavalli, A.; Bui, J. M.; Richter, B.; Dobson, C. M.; Vendruscolo, M. A coupled equilibrium shift mechanism in calmodulin-mediated signal transduction. *Structure* **2008**, *16*, 736−746.

(44) Seaton, B. A.; Head, J. F.; Engelman, D. M.; Richards, F. M. Calcium-induced increase in the radius of gyration and maximum dimension of calmodulin measured by small-angle X-ray scattering. *Biochemistry* **1985**, *24*, 6740−6743.

(45) Heidorn, D. B.; Trewhella, J. Comparison of the crystal and solution structures of calmodulin and troponin C. *Biochemistry* **1988**, *27*, 909−915.

(46) Ogura, K.; Kumeta, H.; Takahasi, K.; Kobashigawa, Y.; Yoshida, R.; Itoh, H.; Yazawa, M.; Inagaki, F. Solution structures of yeast Saccharomyces cerevisiae calmodulin in calcium- and target peptide-bound states reveal similarities and differences to vertebrate calmodulin. *Genes Cells* **2012**, *17*, 159−172.

(47) Bayley, P. M.; Martin, S. R. The alpha-helical content of calmodulin is increased by solution conditions favouring protein crystallisation. *Biochim. Biophys. Acta* **1992**, *1160*, 16−21.

(48) Pandey, K.; Dhoke, R. R.; Rathore, Y. S.; Nath, S. K.; Verma, N.; Bawa, S.; Ashish. Low pH overrides the need of calcium ions for the shape-function relationship of calmodulin: resolving prevailing debates. *J. Phys. Chem. B* **2014**, *118*, 5059−5074.

(49) Bayley, P.; Martin, S.; Jones, G. The conformation of calmodulin: a substantial environmentally sensitive helical transition in Ca_4-calmodulin with potential mechanistic function. *FEBS Lett.* **1988**, *238*, 61−66.

(50) Minnes, L.; Greetham, G. M.; Shaw, D. J.; Clark, I. P.; Fritzsch, R.; Towrie, M.; Parker, A. W.; Henry, A. J.; Taylor, R. J.; Hunt, N. T. Uncovering the Early Stages of Domain Melting in Calmodulin with Ultrafast Temperature-Jump Infrared Spectroscopy. *J. Phys. Chem. B* **2019**, *123*, 8733−8739.

(51) Wyttenbach, T.; Grabenauer, M.; Thalassinos, K.; Scrivens, J. H.; Bowers, M. T. The effect of calcium ions and peptide ligands on the relative stabilities of the calmodulin dumbbell and compact structures. *J. Phys. Chem. B* **2010**, *114*, 437−447.

(52) Anthis, N. J.; Doucleff, M.; Clore, G. M. Transient, sparsely populated compact states of apo and calcium-loaded calmodulin probed by paramagnetic relaxation enhancement: interplay of conformational selection and induced fit. *J. Am. Chem. Soc.* **2011**, *133*, 18966−18974.

(53) Tsvetkov, P. O.; Protasevich, I. I.; Gilli, R.; Lafitte, D.; Lobachov, V. M.; Haiech, J.; Briand, C.; Makarov, A. A. Apocalmodulin binds to the myosin light chain kinase calmodulin target site. *J. Biol. Chem.* **1999**, *274*, 18161−18164.

(54) Kumar, V.; Chichili, V. P.; Zhong, L.; Tang, X.; Velazquez-Campoy, A.; Sheu, F. S.; Seetharaman, J.; Gerges, N. Z.; Sivaraman, J. Structural basis for the interaction of unstructured neuron specific substrates neuromodulin and neurogranin with Calmodulin. *Sci. Rep.* **2013**, *3*, 1392.

(55) Gardill, B. R.; Rivera-Acevedo, R. E.; Tung, C. C.; Van Petegem, F. Crystal structures of Ca^{2+}-calmodulin bound to Na_V C-terminal regions suggest role for EF-hand domain in binding and inactivation. *Proc. Natl. Acad. Sci. U. S. A.* **2019**, *116*, 10763−10772.

(56) Chagot, B.; Chazin, W. J. Solution NMR structure of Apo-calmodulin in complex with the IQ motif of human cardiac sodium channel NaV1.5. *J. Mol. Biol.* **2011**, *406*, 106−119.

(57) Sarhan, M. F.; Van Petegem, F.; Ahern, C. A. A double tyrosine motif in the cardiac sodium channel domain III-IV linker couples calcium-dependent calmodulin binding to inactivation gating. *J. Biol. Chem.* **2009**, *284*, 33265−33274.

(58) Marlow, M. S.; Wand, A. J. Conformational dynamics of calmodulin in complex with the calmodulin-dependent kinase kinase alpha calmodulin-binding domain. *Biochemistry* **2006**, *45*, 8732−8741.

(59) Osawa, M.; Tokumitsu, H.; Swindells, M. B.; Kurihara, H.; Orita, M.; Shibanuma, T.; Furuya, T.; Ikura, M. A novel target recognition revealed by calmodulin in complex with Ca^{2+}-calmodulin-dependent kinase kinase. *Nat. Struct. Biol.* **1999**, *6*, 819−824.

(60) Rellos, P.; Pike, A. C.; Niesen, F. H.; Salah, E.; Lee, W. H.; von Delft, F.; Knapp, S. Structure of the CaMKIIdelta/calmodulin complex reveals the molecular mechanism of CaMKII kinase activation. *PLoS Biol.* **2010**, *8*, No. e1000426.

(61) Clapperton, J. A.; Martin, S. R.; Smerdon, S. J.; Gamblin, S. J.; Bayley, P. M. Structure of the complex of calmodulin with the target sequence of calmodulin-dependent protein kinase I: studies of the kinase activation mechanism. *Biochemistry* **2002**, *41*, 14669−14679.